Numerical Heat Transfer, Part A, 56: 301–324, 2009

ISSN: 1040-7782 print/1521-0634 online
DOI: 10.1080/10407780903244346

Taylor & Francis
Taylor & Francis Group

TURBULENT FLOW IN WAVY CHANNELS SIMULATED WITH NONLINEAR MODELS AND A NEW IMPLICIT FORMULATION

Marcelo Assato and Marcelo J. S. de Lemos
Departamento de Energia–IEME, Instituto Tecnológico de Aeronáutica–ITA, Sao Paulo, Brazil

This work examines the performance of linear and nonlinear eddy-viscosity models when used to predict the turbulent flow in periodically sinusoidal-wave channels. Two geometries are investigated, namely a converging-diverging channel and a channel with concave-convex walls. The numerical method employed for the discretization of the equations is the control-volume method in a boundary-fitted nonorthogonal coordinate system. The SIMPLE algorithm is used for correcting the pressure field. The classical wall function and a low Reynolds model are used to describe the flow near the wall. Comparisons between those two approaches using linear and nonlinear turbulence models are done. Here, a new implicit numerical treatment is proposed for the nonlinear diffusion terms of the momentum equations in order to increase the robustness. Results show that by decomposing and treating terms as presented, solutions using nonlinear models and the high Reynolds wall treatment, which combine accuracy and economy, are more stable and easier to be obtained.

INTRODUCTION

The analysis of flow over wavy boundaries and time-varying boundary conditions is of great interest in engineering and has motivated a number of recent studies, including flow in corrugated ducts [1–5], in spatially periodic channels [6, 7], and with time-oscillating or spatially-varying boundary conditions [8–12]. Further, several phenomena involving wavy boundaries occur in nature, such as generation of wind waves over water, evolution of sand dunes in deserts, and sediment dunes in rivers, to mention a few [13]. Some industrial devices make use of sinusoidal walls as well. Development of high-performance thermal systems has received much attention recently. Modified surfaces are required to reduce the size and weight of heat exchange devices such as those encountered in electronic cooling, air-conditioning, automobiles, aircrafts, spacecrafts, etc.

According to Habib et al. [14], there are many different ways of increasing heat and mass transfer using distinct surfaces for generating turbulence (zigzag-type,

Received 29 September 2008; accepted 3 July 2009.

The authors would like to thank CNPq and CAPES, Brazil, for their invaluable continuous support during the preparation of this work.

Address correspondence to Marcelo J. S. de Lemos, Departamento de Energia–IEME, Instituto Tecnológico de Aeronáutica–ITA, 12228-900 São José dos Campos, SP., Brazil. E-mail: delemos@ita.br

NOMENCLATURE

c_μ	coefficient of turbulent model	y	coordinate normal to the streamwise direction
c_1, c_2	constants in turbulent model	ε	dissipation rate of k, $\nu\overline{(\partial u_i'/\partial k_i')(\partial u_j'\partial x_j)}$
c_{1NL}, c_{2NL}, c_{3NL}	coefficients of nonlinear terms	$\eta - \xi$	generalized coordinate
k	turbulent kinetic energy per unit mass, $\overline{u_i'u_i'}/2$	κ	Von Kármán's universal constant
P	mean pressure	μ, μ_t	dynamic viscosity and eddy dynamic viscosity
P_k	production of turbulent kinetic energy	ρ	density of the fluid
s	dimensionless strain	Γ_ϕ	transport coefficient
s_ϕ	source term	σ_k, σ_ε	model constants for turbulent diffusion of k and ε
S_{ij}	strain rate tensor	τ_{ij}	reynolds stress tensor, $-\rho\overline{u_i'u_j'}$
U, V	mean velocity components	τ_w	wall shear stress
x	coordinate in the streamwise direction	Ω	dimensionless vorticity tensor
		Ω_{ij}	vorticity tensor

cavity-type, grooved-type, staggered ribs-type, etc.). Various researchers experimentally studied turbulent flow over wavy boundaries. Hsu and Kennedy [15] investigated axisymmetric flow in a circular pipe where the diameter varied in a sinusoidal form along its length. Zilker et al. [16] and Buckels et al. [17] measured the shear stress and velocity profiles in a channel with a wavy wall at the bottom of a sine shape. Saniei and Dini [18] measured pressure drop, velocity profile, and local heat transfer for the case of periodical converging-diverging rectangular channels using three different aspect ratios and Reynolds number ranging from 10^4 to 10^5. Hanratty et al. [19] numerically studied the turbulent flow in a channel with sinusoidal surface at the bottom and Patel et al. [13] investigated a rectangular channel using different amplitudes. Habib et al. [14] simulated the flow in sinusoidal converging-diverging channel. They used the linear $k-\varepsilon$ model and presented velocity, streamlines, turbulent kinetic energy, pressure drop, friction factor, and local, average, and maximum Nusselt numbers for Re from 4×10^4 to 10^5.

Accordingly, it seems to be accepted in the literature that linear eddy-viscosity turbulence models (LEVM) do not cope well with strong streamline curvature arising from flow over curved surfaces or imparted swirling. Yet, turbulence-driven secondary motion and directional effects due to buoyancy cannot, due to absence of information on individual stresses, be fully simulated with LEVMs. In spite of that, they are often used for engineering computations due to the numerical robustness obtained via its linear stress-strain rate relationship [20]. This diffusion-like approach makes the numerical solution stable, with the model easily adaptable to existing computer code architectures. Models involving other types of constitutive equations have been lately developed with the perspective of applying CFD to complex flows. These techniques aim at a wider range of applicability, similar to that of Reynolds stress models [21] while keeping computational costs down to LEVM cost levels. Theories employing other type of representation of individual Reynolds stresses/fluxes, including addition of nonlinear terms to the basic constitutive equation, try to

capture the sensitivity to flow curvatures and buoyancy, a feature missing in basic LEVMs.

To the best of the authors' knowledge, most published work on nonlinear models [22–26] are either written for Cartesian coordinates and/or treat additional nonlinear terms in a fully explicit manner. The literature refers to the difficulties of convergence of the solution when nonlinear turbulence models are used in complex flows [27–29]. Here, a *new* numerical treatment is proposed to handle a general nonlinear constitutive equation into a boundary-fitted computer code. Nonlinear diffusion fluxes are linearized for increase of robustness of the method. Common practices in the literature simply treat those additional terms as sources, reducing relaxation parameters to avoid divergent solutions. Therefore, the numerical methodology proposed herein contributes to the robustness of the solution method and increases the applicability of such nonlinear models to numerical grids fully complacent with irregular computational domains. The treatment consists in splitting the nonlinear diffusive fluxes in an implicit term in the coefficients matrix, as well as an explicit part hold in the source term.

None of the publications above reviewed compared different turbulence models when analyzing the flow, which is the subject of this contribution. Further, there seems to be no published proposal like the one here, which is related to a new attempt to discretized the flow equations in order to enhance the degree of implicitness of the numerical solution. Therefore, the objective of this work is two-fold: 1) to investigate the computational robustness of a new implicit numerical treatment for nonlinear diffusion terms, and 2) to analyze the performance of linear and nonlinear eddy-viscosity models in predicting turbulent flow in periodical sinusoidal-wave channels, using both the classical wall function and low Reynolds damping functions for handling wall proximity.

MEAN AND TURBULENT FIELDS

The governing equations to be solved are the continuity and the Reynolds-averaged Navier-Stokes equations, which take the following form:

$$\frac{\partial U_i}{\partial x_i} = 0 \tag{1}$$

$$\rho U_j \frac{\partial U_i}{\partial x_j} = \frac{\partial \tau_{ij}}{\partial x_j} - \frac{\partial P}{\partial x_i} \tag{2}$$

where U_i is the mean velocity component in the i-direction, and ρ is the density of the fluid. For ease of computation, the total pressure $P = p + \frac{2}{3}\rho k$ also involves a term containing the turbulent kinetic energy $k = \overline{u_i' u_i'}/2$ where u_i' is the fluctuating part of the instantaneous velocity in the i-direction. The stress τ_{ij} represents the sum of the turbulent stress, τ_{ij}^t, plus the laminar viscous stress, $\tau_{ij}^\ell = \mu S_{ij}$, where the deformation tensor is given by

$$\mathrm{S}_{ij} = \left(\frac{\partial U_i}{\partial x_j} + \frac{\partial U_j}{\partial x_i} \right) \tag{3}$$

Different constitutive equations for the Reynolds stress will be discussed later and they shall be classified basically in linear and nonlinear relationships.

The modeled transport equations for the turbulent kinetic energy k and its dissipation rate ε, respectively, are given by

$$U_i \frac{\partial k}{\partial x_i} = \frac{\partial}{\partial x_i}\left(\frac{\mu_t}{\rho\sigma_k}\frac{\partial k}{\partial x_i}\right) + P_k - \varepsilon \tag{4}$$

$$U_i \frac{\partial \varepsilon}{\partial x_i} = \frac{\partial}{\partial x_i}\left(\frac{\mu_t}{\rho\sigma_\varepsilon}\frac{\partial \varepsilon}{\partial x_i}\right) + c_1 \frac{\varepsilon}{k} P_k - c_2 f_2 \frac{\varepsilon^2}{k} \tag{5}$$

The symbols P_k and μ_t, respectively, represent the turbulence kinetic energy production rate and the eddy viscosity, and are defined as

$$P_k = \tau_{ij}^t \frac{\partial U_i}{\partial x_j}, \quad \mu_t = c_\mu f_\mu \rho \frac{k^2}{\varepsilon} \tag{6}$$

In the present work, both high and low Reynolds models are compared. Their basic difference lies in the distinct form of the damping functions f_2 and f_μ, with distinct expressions for them, shown in Table 1 [30]. When calculating the wall shear stress with the high Reynolds method [31], E in Table 1 may be varied to simulate the surface roughness. Also, $\kappa = 0.41$ is the numerical value used for the von Kármán constant and subscript P refers to the node next to the wall. Thus, u_P and k_P are, respectively, the value of the velocity and turbulent kinetic energy in this point, and y_P is the normal distance to the wall. The symbol n in the low Reynolds model represents the normal distance to the wall. The constants c_μ, c_1, c_2, σ_k, and σ_ε for the high Reynolds model are set as 0.09, 1.44, 1.92, 1.0, and 1.33, respectively, and for the low Reynolds model given by 0.09, 1.5, 1.9, 1.4, and 1.3, respectively.

Table 1. High and low Reynolds models

	High Reynolds model proposed by Launder and Spalding [31]	Low Reynolds model proposed by Abe et al. [30]
f_μ	1.0	$\left\{1 - \exp\left[-\frac{(\nu\varepsilon)^{0.25} n}{14\nu}\right]\right\}^2 \left\{1 + \frac{5}{(k^2/\nu\varepsilon)^{0.75}} \exp\left[-\left(\frac{(k^2/\nu\varepsilon)}{200}\right)^2\right]\right\}$
f_2	1.0	$\left\{1 - \exp\left[-\frac{(\nu\varepsilon)^{0.25} n}{3.1\nu}\right]\right\}^2 \left\{1 - 0.3 \exp\left[-\left(\frac{(k^2/\nu\varepsilon)}{6.5}\right)^2\right]\right\}$
τ_w	$\frac{u_P \rho c_\mu^{\frac{1}{4}} \kappa k_P^{\frac{1}{2}}}{\ln\left(\frac{E\rho c_\mu^{\frac{1}{4}} k_P^{\frac{1}{2}} y_P}{\mu}\right)}$	$\mu \frac{\partial u}{\partial y}$

In this work, the linear and nonlinear eddy-viscosity models are analyzed. For the linear $k-\varepsilon$ model of turbulence, the Reynolds stress tensor is assumed to be of the following form:

$$\tau_{ij}^{t} = \mu_t S_{ij} - \frac{2}{3}\rho\delta_{ij}k \tag{7}$$

As mentioned before, the last term in Eq. (7) was compacted into an expression for the total pressure P.

Nonlinear eddy-viscosity models originated in a general proposal done by Pope [32]. However, only in the past two decades such models have had great progresses with the works of references [22–25], among others. In these works, quadratic products were introduced involving the strain and vorticity tensors with different derivations and calibrations for the models. These quadratic forms produce a certain anisotropy degree among the normal tensions, which make possible to predict, among other processes, the presence of secondary motion in noncircular ducts.

A general nonlinear expression for the Reynolds stress, kept to second order, can be written as

$$\begin{aligned}\tau_{ij}^{t} = {} & \left(\mu_t S_{ij}\right)^{L} - \left(c_{1NL}\mu_t \frac{k}{\varepsilon}\left[S_{im}S_{mj} - \frac{1}{3}S_{ml}S_{ml}\delta_{ij}\right]\right)^{\mathrm{NL1}} \\ & - \left(c_{2\mathrm{NL}}\mu_t \frac{k}{\varepsilon}\left[\Omega_{im}S_{mj} + \Omega_{jm}S_{mi}\right]\right)^{\mathrm{NL2}} \\ & - \left(c_{3\mathrm{NL}}\mu_t \frac{k}{\varepsilon}\left[\Omega_{im}\Omega_{jm} - \frac{1}{3}\Omega_{lm}\Omega_{lm}\delta_{ij}\right]\right)^{\mathrm{NL3}}\end{aligned} \tag{8}$$

or

$$\tau_{ij}^{t} = \tau_{ij}^{L} + \tau_{ij}^{\mathrm{NL1}} + \tau_{ij}^{\mathrm{NL2}} + \tau_{ij}^{\mathrm{NL3}} \tag{9}$$

where the c's are constants or coefficients, δ_{ij} is the Kronecker delta, the superscripts in equations above indicate linear and nonlinear contributions, S_{ij} is the deformation tensor given by Eq. (3) and Ω_{ij} represents the vorticity tensor written as

$$\Omega_{ij} = \left(\frac{\partial U_i}{\partial x_j} - \frac{\partial U_j}{\partial x_i}\right) \tag{10}$$

Equation (8) already assumes that the term $\frac{2}{3}\rho\delta_{ij}k$ is combined into the total pressure P. In this work, the nonlinear model proposed by Shih et al. [25] was used and has the following expressions.

$$c_\mu = \frac{2/3}{1.25 + s + 0.9\Omega},\ c_{1\mathrm{NL}} = \frac{0.75}{c_\mu(1000 + s^3)},$$
$$c_{2\mathrm{NL}} = \frac{3.8}{c_\mu(1000 + s^3)},\ c_{3\mathrm{NL}} = \frac{4.8}{c_\mu(1000 + s^3)}$$

where

$$s = \frac{k}{\varepsilon}\sqrt{\frac{1}{2}S_{ij}S_{ij}} \quad \text{and} \quad \Omega = \frac{k}{\varepsilon}\sqrt{\frac{1}{2}\Omega_{ij}\Omega_{ij}} \tag{11}$$

NUMERICAL METHOD AND PROCEDURE

Figure 1 shows a typical control-volume with detailed notation, distances, and indexing used when transforming the original equations into the $\eta - \xi$ coordinate system. Boundary conditions for the channel included periodic flow at entrance and exit in Figure 2 and nonslip conditions at the walls.

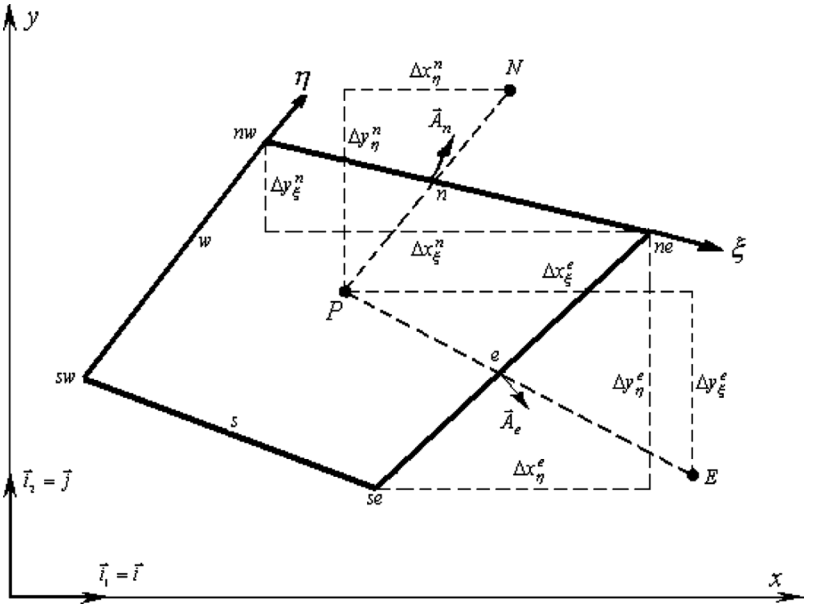

Figure 1. Control-volume and notation.

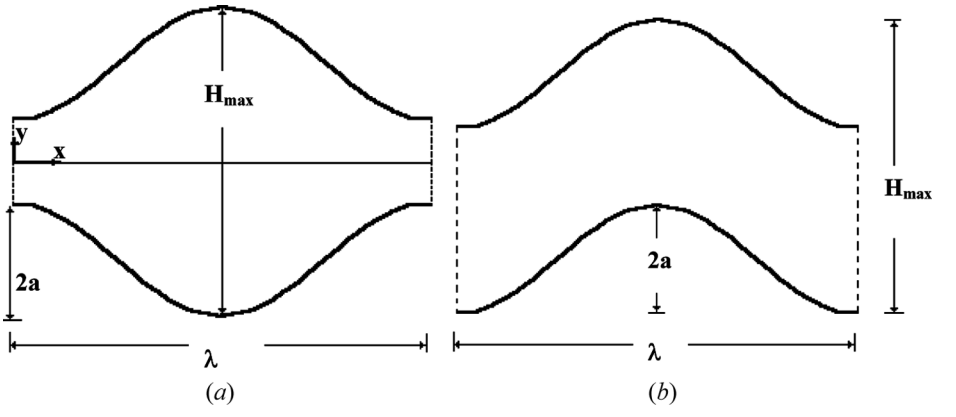

Figure 2. Geometries of periodically sinusoidal-wave channels. (*a*) Symmetric converging-diverging channel and (*b*) channel with concave-convex walls.

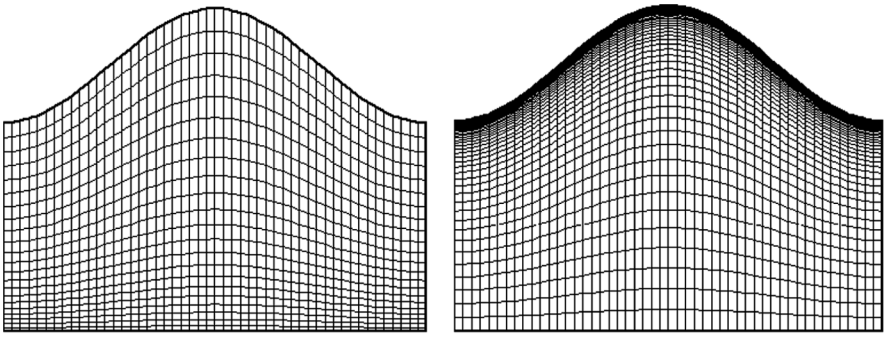

Figure 3. Computational grids of symmetric converging-diverging channel for $2a/\lambda = 0.27$. (*a*) High Reynolds model (50×22) and (*b*) low Reynolds model (50×46).

The grids in Figure 3 were generated using a boundary fitted nonorthogonal coordinated system. The equations above were discretizing using the control-volume approach [33] applied over the generated collocated grid. Pressure-velocity coupling was handled by the SIMPLE method [33]. A hybrid scheme, upwind differencing scheme (UDS) and central differencing scheme (CDS), was used for interpolating the convection fluxes. The system of algebraic equation were relaxed using the strong implicit procedure by Stone [41]. Convergence was monitored in terms of the normalized residue for each variable. The maximum residue allowed for convergence check was set to 10^{-6}, being the variables normalized by appropriate reference values. Constraints for turbulent flows in porous media are similar to the clear channel flow.

For the high Reynolds model, damping functions f_μ, f_2 in Eqs. (5) and (6) take the null value, and the wall shear stress τ_w is calculated using the wall log-law (Table 1) instead of having grid nodes inside the viscous-affected wall region (Figure 3*a*). For the low Reynolds model, detailed computations are performed close to the wall using more nodal points as the wall is approached, so that the viscous sublayer and the buffer zone are resolved (Figure 3*b*).

NOVEL SEMI-IMPLICIT TREATMENT

Although it is recognized that the use of well established algorithms do not characterize a novelty by itself, one should point our that the main idea here is to propose a new treatment when solving the discretized diffusion terms rather than optimizing known algorithms. Also, the work herein aims at increasing the robustness of the numerical method without resorting to techniques that operate simultaneously on more than one dependent variable, as is the case of block-implicit methods [34–36]. Here, implicit handling of individual momentum equations is considered.

With the help of Figure 1, the following operators can be identified.

$$\Delta x^e_\eta = (x_{ne} - x_{se}),\ \Delta x^e_\xi = (x_E - x_P),\ \Delta y^e_\eta = (y_{ne} - y_{se}),\ \Delta y^e_\xi = (y_E - y_P) \tag{12}$$

$$\Delta x^n_\xi = (x_{ne} - x_{nw}),\ \Delta x^n_\eta = (x_N - x_P),\ \Delta y^n_\xi = (y_{ne} - y_{nw}),\ \Delta y^n_\eta = (y_N - x_P) \tag{13}$$

$$\Pi_e = \Delta y^e_\eta \Delta x^e_\xi - \Delta y^e_\xi \Delta x^e_\eta$$

$$\Delta U^e_\xi = (U_E - U_P);\ \Delta U^e_\eta = (U_{ne} - U_{se}) \tag{14}$$

$$\Delta V^e_\xi = (V_E - V_P);\ \Delta V^e_\eta = (V_{ne} - V_{se}) \tag{15}$$

$$\pi^e_a = \Delta y^e_\eta (U_E - U_P) - \Delta y^e_\xi (U_{ne} - U_{se}) = \Delta y^e_\eta \Delta U^e_\xi - \Delta y^e_\xi \Delta U^e_\eta$$

$$\pi^e_b = \Delta x^e_\xi (U_{ne} - U_{se}) - \Delta x^e_\eta (U_E - U_P) = \Delta x^e_\xi \Delta U^e_\eta - \Delta x^e_\eta \Delta U^e_\xi$$

$$\pi^e_c = \Delta y^e_\eta (V_E - V_P) - \Delta y^e_\xi (V_{ne} - V_{se}) = \Delta y^e_\eta \Delta V^e_\xi - \Delta y^e_\xi \Delta V^e_\eta$$

$$\pi^e_d = \Delta x^e_\xi (V_{ne} - V_{se}) - \Delta x^e_\eta (V_E - V_P) = \Delta x^e_\xi \Delta V^e_\eta - \Delta x^e_\eta \Delta V^e_\xi \tag{16}$$

Further, the vector form of the area of the control-volume at east and north faces, respectively, are given by

$$\vec{A}_e = \Delta y^e_\eta \vec{i} - \Delta x^e_\eta \vec{j} \qquad \vec{A}_n = -\Delta y^n_\xi \vec{i} + \Delta x^n_\xi \vec{j} \tag{17}$$

Governing Equations

For a general dependent variable φ a discrete form of Eqs. (1), (2), (4), and (5) can be written as:

$$I_e + I_w + I_n + I_s = S_\varphi \tag{18}$$

where I_e, I_w, I_n, and I_s are the overall fluxes (convection plus diffusion) of φ at the east, west, north, and south control-volume faces, respectively, and S_φ is the corresponding source term.

For the east face the total flux can be written for a general variable $\vec{\varphi}$ as

$$I_e = \int_{A_e} (\vec{n} \cdot \vec{\varphi}) dA \approx (\vec{n}_e \cdot \vec{\varphi}_e) A_e \tag{19}$$

where A_e is the control-volume east face area, $\vec{n}_e$ is the unit vector normal to A_e, and $\vec{\varphi}_e$ is the average value of $\vec{\varphi}$ prevailing over A_e. Also, for coherence in the discretization process, the continuity of fluxes at any interface implies that

$$(I_w)_P = -(I_e)_W \qquad (I_s)_P = -(I_n)_S \tag{20}$$

The numerical treatment of convection and diffusion mechanisms is handled separately. When Eq. (18) is written for the x-direction, the convective flux, I^{C_x}, has contributions from both faces east e and north n in the following way.

$$I^{C_x}_e \approx F_e U_e \qquad I^{C_x}_n \approx F_n U_n \tag{21}$$

where

$$F_e = \rho[U_e \Delta y^e_\eta - V_e \Delta x^e_\eta]$$
$$F_n = \rho[V_n \Delta x^n_\xi - U_n \Delta y^n_\xi] \tag{22}$$

The flux blended deferred correction scheme [37], indicated here as DCS, is employed to perform nodal interpolation. In this scheme, interface quantities are approximated as linear combination of central differencing scheme (CDS) and upwind differencing scheme (UDS) values [33] according to

$$\phi^{\mathrm{DCS}}_{\mathrm{face}} = \lambda \phi^{\mathrm{CDS}}_{\mathrm{face}} + (1-\lambda)\phi^{\mathrm{UDS}}_{\mathrm{face}} = \phi^{\mathrm{UDS}}_{\mathrm{face}} + \lambda\left(\phi^{\mathrm{CDS}}_{\mathrm{face}} - \phi^{\mathrm{UDS}}_{\mathrm{face}}\right)^o \tag{23}$$

where the quantities with superscript o in parenthesis (last equality) are numerical values from the previous iteration. The interpolation factor λ may vary from 0 (pure UDS) to 1 (pure CDS).

For the diffusive flux in the same x-direction, I^{D_x}, both faces are also considered.

$$I^{D_x}_e \approx -(\tau_{11}\vec{i} + \tau_{12}\vec{j})_e \cdot \vec{A}_e \tag{24}$$
$$I^{D_x}_n \approx -(\tau_{11}\vec{i} + \tau_{12}\vec{j})_n \cdot \vec{A}_n \tag{25}$$

Here, in accordance with Eq. (9), the diffusion flux in each face for each direction can be split into linear and nonlinear parts as

$$\begin{aligned} I^{D_x}_e = &-(\tau_{11}\vec{i} + \tau_{12}\vec{j})^L_e \cdot \vec{A}_e - (\tau_{11}\vec{i} + \tau_{12}\vec{j})^{\mathrm{NL1}}_e \cdot \vec{A}_e \\ &- (\tau_{11}\vec{i} + \tau_{12}\vec{j})^{\mathrm{NL2}}_e \cdot \vec{A}_e - (\tau_{11}\vec{i} + \tau_{12}\vec{j})^{\mathrm{NL3}}_e \cdot \vec{A}_e \end{aligned} \tag{26}$$

or

$$I^{D_x}_e = \left(I^{D_x}_e\right)^L + \left(I^{D_x}_e\right)^{\mathrm{NL1}} + \left(I^{D_x}_e\right)^{\mathrm{NL2}} + \left(I^{D_x}_e\right)^{\mathrm{NL3}} \tag{27}$$

Likewise, for the north face,

$$I^{D_x}_n = \left(I^{D_x}_n\right)^L + \left(I^{D_x}_n\right)^{\mathrm{NL1}} + \left(I^{D_x}_n\right)^{\mathrm{NL2}} + \left(I^{D_x}_n\right)^{\mathrm{NL3}} \tag{28}$$

Thus, a discrete form for Eq. (27) will be

$$\left(I^{D_x}_e\right)^{\mathrm{L}} = -\frac{\mu^e_t}{\Pi_e}\{\Delta U^e_\xi[2(\Delta y^e_\eta)^2 + (\Delta x^e_\eta)^2] - \Delta U^e_\eta[2\Delta y^e_\xi \Delta y^e_\eta + \Delta x^e_\xi \Delta x^e_\eta] - \pi^e_c \Delta x^e_\eta\} \tag{29}$$

$$\left(I^{D_x}_e\right)^{\mathrm{NL1}} = \frac{c_{1\mathrm{NL}}\mu^e_t k}{(\Pi_e)^2 \varepsilon}\left\{-\Delta y^e_\eta\left[\frac{8}{3}\left(\pi^e_a\right)^2 + \frac{1}{3}\left(\pi^e_b + \pi^e_c\right)^2 - \frac{4}{3}\left(\pi^e_d\right)^2\right] + 2\Delta x^e_\eta\left[\left(\pi^e_a + \pi^e_d\right)\left(\pi^e_b + \pi^e_c\right)\right]\right\} \tag{30}$$

$$\left(I^{D_x}_e\right)^{\mathrm{NL2}} = 2c_{2\mathrm{NL}}\frac{\mu^e_t}{(\Pi_e)^2}\frac{k}{\varepsilon}\left\{-\Delta y^e_\eta\left[(\pi^e_b)^2 - (\pi^e_c)^2\right] + \Delta x^e_\eta[(\pi^e_d - \pi^e_a)(\pi^e_b - \pi^e_c)]\right\} \tag{31}$$

$$\left(I_e^{D_x}\right)^{\mathrm{NL3}} = c_{3\mathrm{NL}} \frac{\mu_t^e}{(\Pi_e)^2} \frac{k}{\varepsilon} \left\{ -\Delta y_\eta^e \left[\frac{1}{3} (\pi_b^e - \pi_c^e)^2 \right] \right\} \tag{32}$$

where the velocity difference operators are defined by Eqs. (14) and (15). At north face n the diffusive fluxes have an analogous form. For the y-momentum equation, the diffusive fluxes at both east and north faces are also obtained in a similar fashion.

In the numerical treatment presented by references [38–40], as well as in the majority of similar nonlinear calculations in the literature, the diffusion term was totally explicit in the sense that all terms in Eq. (28) were accommodated into the source term. In the present work, a different methodology is proposed, as shown below.

New Semi-Implicit Treatment for Diffusive Terms

It is a well known feature in the literature that increasing the degree of solution implicitness the robustness of the relaxation process is enhanced [33]. Source term linearization is a common practice among CFD practitioners and, at the end, intends to increase the main diagonal dominance of the matrix of coefficients.

Accordingly, to improve numerical stability, the diffusive terms given by Eqs. (29)–(32) are further rewritten as a combination of implicit and explicit parts in the following form.

$$\left(I_e^{D_x}\right)^{L} = -\Delta U_\xi^e \left(D_e^{x,y}\right)^{L} + \left(S_e^{*_x}\right)^{L} \tag{33}$$

$$\left(I_e^{D_x}\right)^{\mathrm{NL1}} = \Delta U_\xi^e \left(D_e^{x,y}\right)^{\mathrm{NL1}} + \left(S_e^{*_x}\right)^{\mathrm{NL1}} \tag{34}$$

$$\left(I_e^{D_x}\right)^{\mathrm{NL2}} = \Delta U_\xi^e \left(D_e^{x,y}\right)^{\mathrm{NL2}} + \left(S_e^{*_x}\right)^{\mathrm{NL2}} \tag{35}$$

$$\left(I_e^{D_x}\right)^{\mathrm{NL3}} = \Delta U_\xi^e \left(D_e^{x,y}\right)^{\mathrm{NL3}} + \left(S_e^{*_x}\right)^{\mathrm{NL3}} \tag{36}$$

where the velocity difference operator, ΔU_ξ^e, is defined in Eq. (14). Equations (33)–(36) are written for the x-component diffusion flux of the east face of Figure 1 and basically represent the main idea on source linearization discussed in reference [33]. Similar expressions can be written for all other faces and for the y-component of the diffusion flux. It is interesting to emphasize that even for a standard linear model, source term linearization given by reference (33) applies.

The first term on the right hand side of Eqs. (33)–(36) is the term treated implicitly and the second one that it handled in as explicit form. The coefficient $D_e^{x,y}$ is the same for both equations in x and y components and is given by

$$D_e^{x,y} = \left(D_e^{x,y}\right)^{L} + \left(D_e^{x,y}\right)^{\mathrm{NL1}} + \left(D_e^{x,y}\right)^{\mathrm{NL2}} + \left(D_e^{x,y}\right)^{\mathrm{NL3}} \tag{37}$$

where

$$\left(D_e^{x,y}\right)^{L} = \frac{(\mu + \mu_t^e)}{\Pi_e} \left[(\Delta y_\eta^e)^2 + (\Delta x_\eta^e)^2 \right] \tag{38}$$

$$\left(D_e^{x,y}\right)^{\mathrm{NL1}} = c_{1\mathrm{NL}} \frac{\mu_t^e}{(\Pi_e)^2} \frac{k}{\varepsilon} \left\{ -2(\Delta y_\eta^e)^2 \pi_a^e + 2\Delta x_\eta^e \left[\frac{4}{3} \Delta y_\eta^e (\pi_b^e + \pi_c^e) - \Delta x_\eta^e \pi_d^e \right] \right\} \tag{39}$$

$$\left(D_e^{x,y}\right)^{\mathrm{NL2}} = 2c_{2\mathrm{NL}} \frac{\mu_t^e}{(\Pi_e)^2} \frac{k}{\varepsilon} \{ \Delta x_\eta^e \Delta y_\eta^e [\Delta x_\xi^e \Delta U_\eta^e - \Delta y_\xi^e \Delta V_\eta^e] \} \tag{40}$$

$$\left(D_e^{x,y}\right)^{\mathrm{NL3}} = c_{3\mathrm{NL}} \frac{\mu_t^e}{(\Pi_e)^2} \frac{k}{\varepsilon} \{ \Delta x_\eta^e \Delta y_\eta^e [(\pi_b^e + \pi_c^e)] \} \tag{41}$$

where ΔV_ξ^e and ΔV_η^e are given in Eq. (15).

As mentioned, by means of Eqs. (33)–(36), enhancement of matrix main diagonal dominance is achieved, contributing to the robustness of the entire numerical relaxation scheme.

The parts treated explicitly S_e^{*x} make use of velocity values at grid points calculated in the previous iteration. For the east face and x-direction one has.

$$(S_e^{*x})^L = -\frac{(\mu + \mu_t)_e}{\Pi_e} \left\{ (\Delta U_\xi^e)^\circ (\Delta y_\xi^e)^2 - (\Delta U_\eta^e)^\circ \left[2\Delta y_\xi^e \Delta y_\eta^e + \Delta x_\xi^e \Delta x_\eta^e \right] - \pi_c^e \Delta x_\eta^e \right\} \tag{42}$$

$$\left(S_e^{*x}\right)^{\mathrm{NL1}} = -\frac{2c_{1\mathrm{NL}}\mu_t^e k}{(\Pi_e)^2 \varepsilon} \left\{ \begin{array}{l} \Delta y_\eta^e \left[\frac{1}{3}(\pi_a^e)^2 + \left(\Delta U_\eta^e\right)^o \left(-\Delta y_\xi^e \pi_a^e + \Delta x_\xi^e \left(\frac{1}{3}\pi_c^e + \frac{1}{6}\Delta x_\xi^e \left(\Delta U_\eta^e\right)^o \right) \right) - \frac{2}{3}(\pi_d^e)^2 + \frac{1}{6}(\pi_c^e)^2 \right] \\ -\Delta x_\eta^e \left[\frac{1}{6}\Delta x_\eta^e \left(\Delta U_\xi^e\right)^o \pi_a^e + \left(\Delta U_\eta^e\right)^o \left(\Delta x_\xi^e \pi_d^e - \Delta y_\xi^e \left(\pi_c^e + \frac{7}{6}\pi_b^e - \frac{1}{6}\Delta x_\xi^e \left(\Delta U_\eta^e\right)^o \right) \right) + \pi_c^e \pi_d^e \right] \end{array} \right\} \tag{43}$$

$$\left(S_e^{*x}\right)^{\mathrm{NL2}} = -\frac{2c_{2\mathrm{NL}}\mu_t^e k}{(\Pi_e)^2 \varepsilon} \left\{ \Delta y_\eta^e \left[\left(\Delta x_\xi^e\right)^2 \left(\left(\Delta U_\eta^e\right)^o \right)^2 - (\pi_c^e)^2 \right] - \Delta x_\eta^e \left[\begin{array}{l} \left(\Delta y_\eta^e\right)^2 \left(\Delta U_\xi^e\right)^o \left(\Delta V_\xi^e\right)^o + \\ (\pi_b^e - \pi_c^e) \left(\Delta y_\xi^e \left(\Delta U_\eta^e\right)^o \right) + \pi_d^e \end{array} \right] \right\} \tag{44}$$

$$\left(S_e^{*x}\right)^{\mathrm{NL3}} = \frac{c_{3\mathrm{NL}}\mu_t^e k}{(\Pi_e)^2 \varepsilon} \left\{ -\frac{\Delta y_\eta^e}{3} \left[\begin{array}{l} \Delta x_\eta^e \left(\pi_b^e + 3\pi_c^e - \Delta x_\eta^e \left(\Delta U_\xi^e\right)^o \right) \left(\Delta U_\xi^e\right)^o - 2\pi_b^e \pi_c^e + (\pi_c^e)^2 \\ + \left(\Delta x_\xi^e\right)^2 \left(\left(\Delta U_\eta^e\right)^o \right)^2 \end{array} \right] \right\} \tag{45}$$

As before, the superscript o of velocity differences indicates that the values are taken from the previous iteration. Here, splitting Eqs. (33)–(36) using coefficients (37)–(41) and explicit terms (42)–(45) represents a new proposal that, to the best of the authors' knowledge, is not found in the open literature.

Final Form of Discretized Momentum Equation

After all fluxes and source terms are incorporated in to the momentum equation, the algebraic equivalent of Eqs. (2), (4), and (5) is finally assembled. Variables at faces (e, w, n, s) and corners (ne, nw, se, sw) are interpolated forming an equation connecting the variable at P with the its neighbor points (see Figure 1). Using expression (23) for interpolation the face values with UDS and CDS formulation, the final form can be written as

$$a_P^{\mathrm{UDS}}\phi_P = \sum_{nb} a_{nb}^{\mathrm{UDS}}\phi_{nb} + S_\phi^* + \lambda\left(\sum_{nb} a_{nb}^{\mathrm{CDS}}\phi_{nb} - a_P^{\mathrm{UDS}}\phi_P\right)^o, \qquad (46)$$

where $\phi = U, V$ and $nb = E, W, N, S$

Coefficients a_P and a_{nb} contain variables in the faces of the control volume obtained by interpolation of their respective nodal points values. For the east face, the coefficient reads

$$a_E^{\mathrm{UDS}} = D_e^{x,y} + \max(-F_e, 0) \qquad (47)$$

$$a_E^{\mathrm{CDS}} = -\max(-F_e, 0) - F_e f_{x,P} \qquad (48)$$

where $D_e^{x,y}$ is calculated by means of Eq. (37), F_e is given by Eq. (22), and f is a interpolation factor defined by (see Figure 1 for details)

$$f_{x,P} = \frac{x_e - x_P}{x_E - x_P} \qquad (49)$$

The source term S_U^* in the x-momentum equation can be assembled as

$$S_U^* = \overbrace{S_e^{*x} - S_w^{*x} + S_n^{*x} - S_s^{*x}}^{\text{Explicit part of linear term}} + \underbrace{\overbrace{S_e^{*x} - S_w^{*x} + S_n^{*x} - S_s^{*x}}^{\text{Explicit part of 1st. nonlinear term}} + \overbrace{S_e^{*x} - S_w^{*x} + S_n^{*x} - S_s^{*x}}^{\text{Explicit part of 2nd. nonlinear term}} + \overbrace{S_e^{*x} - S_w^{*x} + S_n^{*x} - S_s^{*x}}^{\text{Explicit part of 3rd. nonlinear term}}}_{\text{These terms are null for standard linear models}} + \overbrace{S_{P_x}}^{\text{Pressure term}} \qquad (50)$$

where expressions similar to Eqs. (42)–(45) are used at the four control volume faces.

Sensitivity Analysis

Before presenting the numerical results themselves, a discussion on the sensitivity of the discretized terms seems timely. It is important to emphasize that coefficients $\left(D_e^{x,y}\right)^{\mathrm{NL1}}$, $\left(D_e^{x,y}\right)^{\mathrm{NL2}}$, and $\left(D_e^{x,y}\right)^{\mathrm{NL3}}$, given by Eqs. (39)–(41), respectively, have different numerical values on each control volume and depend on geometric distances, within the grid, as well as on the surrounding velocity values. As such, they can be greater or less that zero. On the other hand, the linear coefficient given by

Eq. (38), $\left(D_e^{x,y}\right)^L$, is composed by positive quantities only. Consequently, for positive nonlinear coefficients $\left(D_e^{x,y}\right)^{\mathrm{NL1}}$, $\left(D_e^{x,y}\right)^{\mathrm{NL2}}$, and $\left(D_e^{x,y}\right)^{\mathrm{NL3}}$ the advantages of the implicit treatment here proposed are not be as evident since numerical instabilities might occur during the relaxation process [33]. To make this idea clear, remember that the overall flux I was defined on the left-hand side of Eq. (18), and when transposed to the right for a source-like view, it is written as

$$\overbrace{-\left(I_e^{D_x}\right)^L}^{\text{Source-like term}} = \underbrace{\Delta U_\xi^e}_{U_E-U_P} \overbrace{\left(D_e^{x,y}\right)^L}^{\text{always positive}} \underbrace{-\left(S_e^{*_x}\right)^L}_{\text{Explixit term}} \tag{51}$$

Likewise, when Eq. (34) is written on the right of Eq. (18), one has

$$-\left(I_e^{D_x}\right)^{\mathrm{NL1}} = \underbrace{-\Delta U_\xi^e}_{U_P-U_E} \overbrace{\left(D_e^{x,y}\right)^{\mathrm{NL1}}}^{\text{Less than ``0'' for stability}} \underbrace{-\left(S_e^{*_x}\right)^{\mathrm{NL1}}}_{\text{Explicit term}} \tag{52}$$

A similar argument can be used for expressions (35) and (36) involving $\left(D_e^{x,y}\right)^{\mathrm{NL2}}$ and $\left(D_e^{x,y}\right)^{\mathrm{NL3}}$, respectively.

Therefore, whenever positive values are detected in each control volume for $\left(D_e^{x,y}\right)^{\mathrm{NL1}}$, the diffusive flux in question is handled back in an explicit form. In this case, Eq. (34) is replaced by

$$\left(I_e^{D_x}\right)^{\mathrm{NL1}} = -\Delta U_\xi^e \left\| -\left(D_e^{x,y}\right)^{\mathrm{NL1}}, 0 \right\| + \left(\Delta U_\xi^e\right)^o \left\| \left(D_e^{x,y}\right)^{\mathrm{NL1}}, 0 \right\| + \left(S_e^{*_x}\right)^{\mathrm{NL1}} \tag{53}$$

Similar expressions hold for the second and third nonlinear terms. With all the contributions due to diffusion properly accounted for in the D's coefficients (see Eq. (37)), in light of the restrictions imposed by Eq. (53), the coefficient a_E in Eq. (47) is calculated.

The modifications above due to Eq. (53) affect the way the velocity at the volume faces are calculated when applying the SIMPLE algorithm [33]. In this method, the basic idea is to solve a pressure correction equation derived from the momentum and continuity equations. It can be shown that the resulting pressure correction equation is [33],

$$a_P P'_P = a_W P'_P + a_E P'_P + a_S P'_P + a_N P'_P - S_m \tag{54}$$

where the primes indicate corrections and S_m is known as the mass imbalance. Face velocities, interpolated from values at main nodes, are used to compute S_m in Eq. (54). Therefore, the way the non-linear diffusion term is handled in Eq. (53) will influence computations of this mass source via the momentum equations. This influence, however, tends to decrease as the solution approaches convergence since both sides of Eq. (54) tend to zero.

Also, it is important to emphasize that for Cartesian grids, with $\eta = x$ and $\psi = y$, or meshes with a high degree of orthogonality, the geometric distances Δx^e_η is null or nearly zero, respectively. This term appears in the formulae for the coefficients $\left(D_e^{x,y}\right)^{\mathrm{NL1}}$, $\left(D_e^{x,y}\right)^{\mathrm{NL2}}$, and $\left(D_e^{x,y}\right)^{\mathrm{NL3}}$, Eqs. (39)–(41), respectively. If $\Delta x^e_\eta \approx 0$, only the first term in Eq. (39), if positive, will contribute to the main coefficient in Eq. (46). Therefore, for an orthogonal or quasi-orthogonal grid, Eqs. (39)–(41) become

$$\left(D_e^{x,y}\right)^{\mathrm{NL1}} \approx c_{1\mathrm{NL}} \frac{\mu_t^e k}{(\Pi_e)^2 \varepsilon} \left\{ -2\left(\Delta y_\eta^e\right)^2 \frac{\Delta U_\xi^e}{\Delta x_\xi^e} \right\}; \quad \left(D_e^{x,y}\right)^{\mathrm{NL2}} \approx 0; \quad \left(D_e^{x,y}\right)^{\mathrm{NL3}} \approx 0 \quad (55)$$

RESULTS AND DISCUSSION

The geometries analyzed are shown in Figure 2. The geometrical parameters are the channel height, $H_{\max} = 10.16\,\mathrm{cm}$, the channel wavelength, $\lambda = 6.667\,\mathrm{cm}$, and aspect ratio $2a/\lambda = 0.27$, where a represents the wave amplitude. The results presented in this section were obtained using a total of four different models. The following turbulence closures were applied: the linear and nonlinear k-ε models using the high Reynolds approach, designated here by L_HRN and NL_HRN, respectively, and the same models applying the low Reynolds approximation, named, respectively, by L_LRN and NL_LRN. The nonlinear model employed was the Shih et al. [25] closure. Also, validation of results here presented is done by comparing simulations with experiments by Habib et al. [14] and Saniei and Dini [18]. Inaccuracies of numerical simulations are then better accessed and evaluated when presenting computations along with laboratory measurements of references [14, 18]. To the best of the authors' knowledge, the numerical results herein are considered to be validated and the computer code checked against possible programming errors.

Figures 3 and 4 show the geometries given above and computational grids when using the high and low Reynolds number formulations, respectively. Grid independency studies were carried out in order to assure that calculated flow properties and integral parameters were not affected by the grid size. Due to lack of space, these results are not presented here. Instead, comparisons with experimental data, as shown next, give a view of the accuracy of the results. Roughly, doubling the grid in both direction changes the pressure loss across one section of length $\lambda = 6.667\,\mathrm{cm}$ cm by less than 4%. Grids of sizes given in Figures 4 were then assumed to suffice for evaluating the implicit procedure here proposed.

Comparisons for the pressure drop along one section of the duct with length $\lambda = 6.667\,\mathrm{cm}$ of the symmetric converging-diverging channel considering the present calculations and the experimental data by Saniei and Dini [18] are shown in Table 2. When simulations are compared to experiments, it can be noticed that smaller deviations appear when using the low Reynolds number formulation. Further, it is also seem that best predictions are obtained by the NL_LRN model using the constitutive Eq. (8) instead of Eq. (7). In this work, calculations were performed only for Reynolds number based on hydraulic diameter of $\mathrm{Re} = 40000$ so that conclusions drawn herein may not be valid for a large range of Re. The reason for liming the

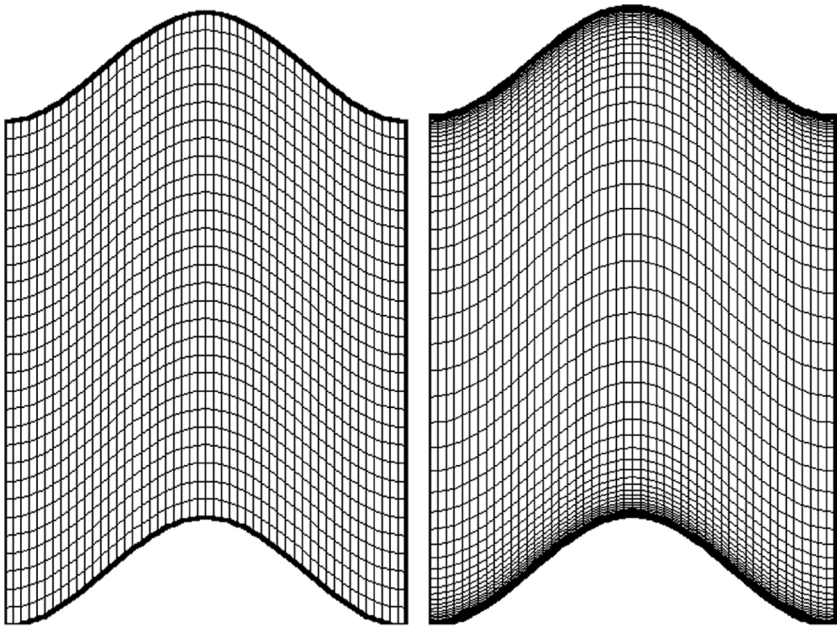

Figure 4. Computational grids of channel with concave-convex walls for $2a/\lambda = 0.27$. (*a*) High Reynolds model (50×28) and (*b*) low Reynolds model (50×58).

Reynolds number is two-fold: to match experimental conditions used by Habib et al. [14], and due to the fact that the main motive of this work is to observe how the proposed implicitness of turbulent diffusion terms, which are calculated with four different models, affects the robustness of the solution. Each one of these models can be sensitive to a wide range of parameters, particularly the Reynolds number and channel dimensions. Sensitivity on Re and/or channel geometry, however, were not the object of this study and shall be the target in future investigations. Here, the proposed implicit treatment is studied in light of the turbulence model applied.

Figure 5 shows the mean velocity field U/U_{avg} in several stations along the converging-diverging channel compared with experiments of Habib et al. [14].

Table 2. Pressure drop for a section of length λ in periodically symmetric converging-diverging channel

Results	Pressure drop ΔP [N/m^2]	Deviations [%]
Saniei and Dini [18]	12.5	—
L_HRN	9.824	−21.4
NL_HRN	10.016	−19.87
L_LRN	11.243	−10.06
NL_LRN	13.553	8.42

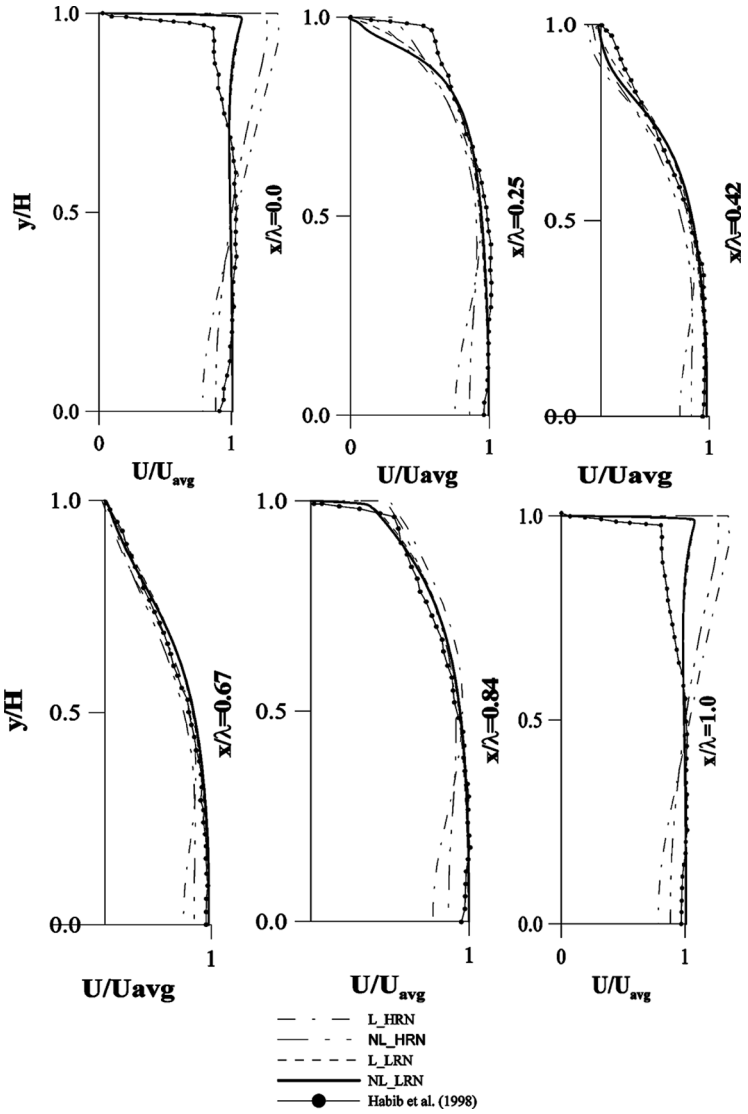

Figure 5. Normalized axial velocity profiles.

All models present small differences among their results, except in first ($x/\lambda = 0$) and last station ($x/\lambda = 1$). These specific positions correspond to the throat at entrance and exit of the periodic section. Due to the periodic boundary conditions here employed, the numerical solution give, as expected, the same calculated values. Included in Figure 5 are the results obtained numerically by Habib et al. [14], which are closer to the ones given by the NL_LRN model. Interesting to note is that measurements at $x/\lambda = 0$ do not perfectly match those at $x/\lambda = 1$, possibly indicating that the flow is still under development or suffering some sort of instability.

Figures 6 and 7 show, respectively, dimensionless axial velocity and turbulent kinetic energy distributions, for the symmetric converging-diverging channel, using the four turbulence models seen before. It can be noticed that bigger deviations among the results occur when changing the wall treatment from high to the low Reynolds number approach, and not so much for the use of more elaborated stress-strain relationships. By that, one mean that when results for HRNs (Figures 6*a*, 6*b*, 7*a*, and 7*b*) are compared with those for LRNs (Figures 6*c*, 6*d*, 7*c*, and 7*d*), differences are greater than when solutions are compared for the same model class (HRN or LRN) and different type of stress-stain relation (linear or nonlinear). The difference between HRN and LRN models lies in the use of distinct damping functions f_μ, f_2 in Eqs. (5) and (6), and the use of different formulae for the wall shear stress τ_w (see Table 1 for comparison). Consequently, the number of grid points close to the wall will differ substantially whether one is bypassing the wall viscous layer (Figures 3*a* and 4*a*), or else one is computing the fine flow by clustering computational nodes inside the wall viscous region (Figures 3*b* and 4*b*). On the other hand, the use of linear or nonlinear expressions for τ_t, Eqs. (7) and (8), respectively, will not affect the solution as much as the wall treatment does (HRN or LRN). This can be clearly seen when comparing the flow pattern in Figures 6*a* and 6*b* for HRN (or Figures 6*c* and 6*d* for LRN), with Figures 6*a*

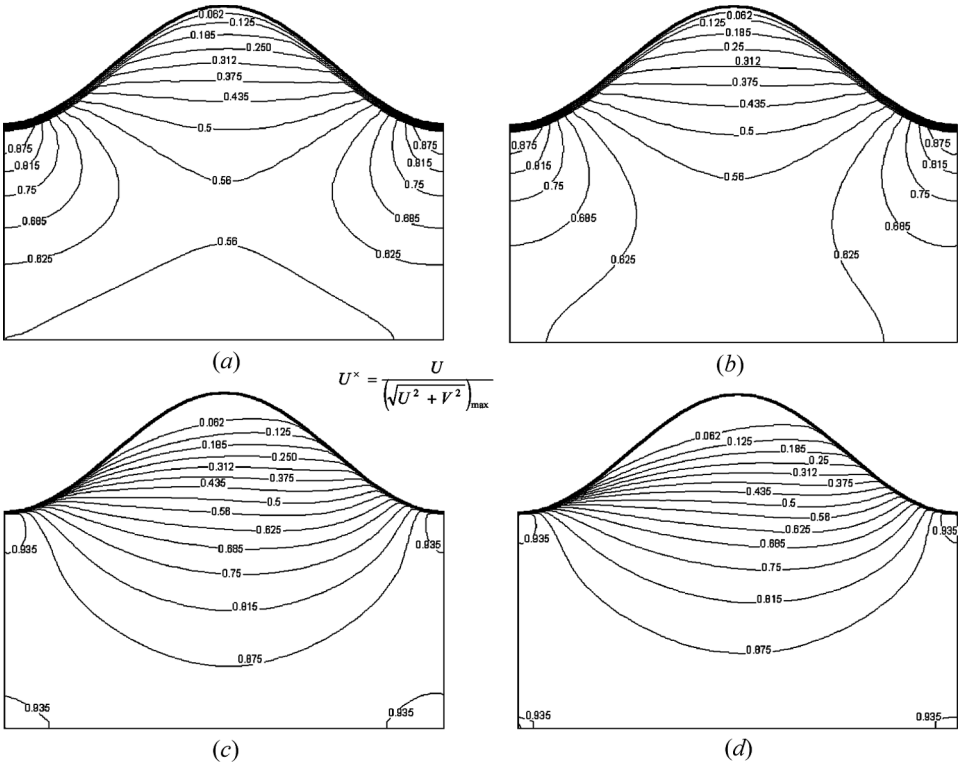

Figure 6. Dimensionless velocity distribution U for the symmetric converging-diverging channel. (*a*) L_HRN; (*b*) NL_HRN; (*c*) L_LRN; and (*d*) NL_LRN.

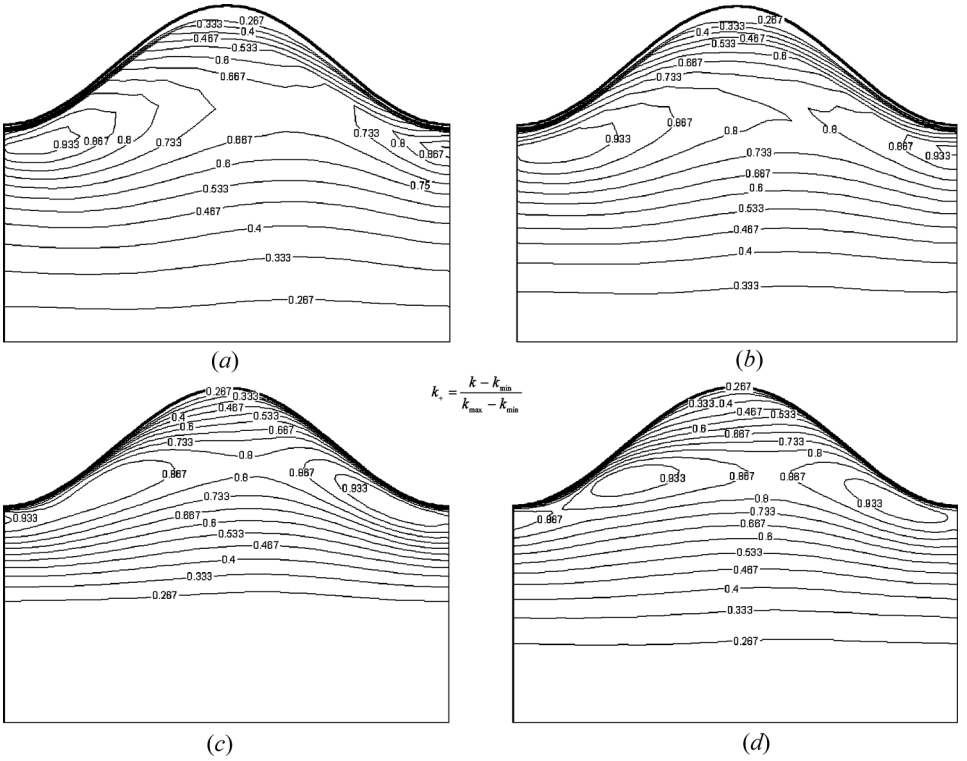

Figure 7. Dimensionless k distribution for the symmetric converging-diverging channel. (*a*) L_HRN; (*b*) NL_HRN; (*c*) L_LRN; and (*d*) NL_LRN.

and 6*c* for linear models (or with Figures 6*b* and 6*d* for nonlinear models). Therefore, the way the wall region is handled, using either a wall-log law (HRN) or a fine grid close to the wall (LRN), affects the results to a greater extent than computing the flow using distinct models for τ_t , Eqs. (7) or (8). In fact, for internal flows the location of the first grid node close to the wall greatly affects the solutions when the HRN is applied [42]. This is because this first nodal point has to located outside the viscous sublayer, in the fully turbulent region, so that the use of a wall law is applicable. Therefore, when using HRN with accelerating and decelerating flows in the periodic channels of Figure 2, such effect might be even more pronounced since the boundary layers is enlarged in decelerating flows and compressed when the flow is pushed towards the wall. As such, control over the first grid point location seems to be more involving when HRN is applied in ducts with accelerating/decelerating flows. The same behavior is observed for the channel with concave-convex walls shown in Figures 8 and 9.

An evaluation on residue histories seems timely for identifying under which circumstances the explicit treatment here proposed give some advantage on the overall solution process. To this end, Figure 10 shows residue history for U along the solution relaxation process, for the symmetric converging-diverging channel, using

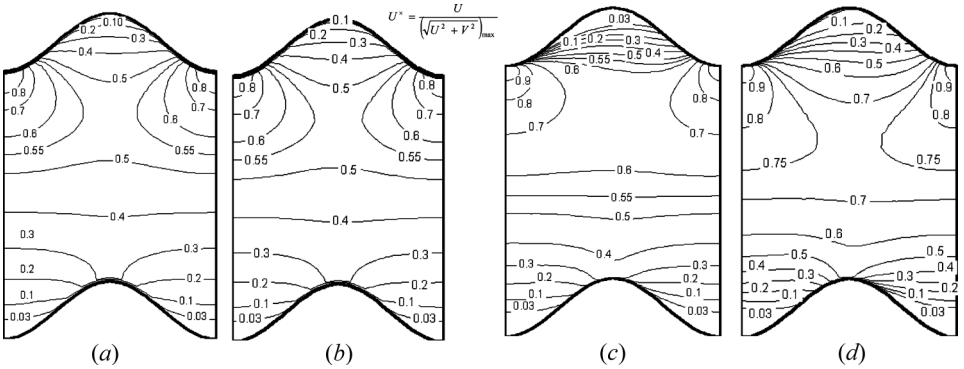

Figure 8. Dimensionless velocity distribution U for the channel with concave-convex walls. (*a*) L_HRN; (*b*) NL_HRN; (*c*) L_LRN; and (*d*) NL_LRN.

the NL_HRN and NL_LRN models. In the figure, calculations using the semi-implicit approach of Eqs. (34)–(36) were employed in addition to having all non-linear diffusive terms being treated in an explicit form. For this case, convergence is easily achieved regardless of the method used and the semi-implicit technique did not benefit the overall stability of the solution. Although not shown in Figure 10, the explicit formulation converged at a rate similar to the one obtained with the semi-implicit approach. Also interesting to note is the much higher computer effort is demanding when using Low Reynolds model. Nearly ten times as much iterations are necessary to bring down residues at the same levels as those in Figure 10*a*. Overall, Figure 10 has the purpose of showing that not all cases require a high degree of implicitness is necessary for convergence to be achieved.

Finally, Figure 11 shows residue histories for the solution of the flow in the concave-convex wall channel of Figure 2*b* using both the NL_HRN and NL_LRN models. Great difficulty was observed for this particular geometry and a large number of iterative cycles were necessary for the turbulent flow to achieve the fully

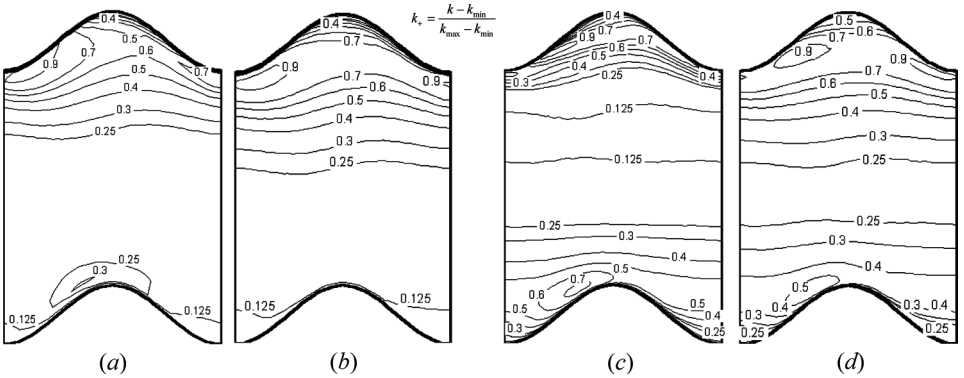

Figure 9. Dimensionless k distribution for the channel with concave-convex walls. (*a*) L_HRN; (*b*) NL_HRN; (*c*) L_LRN; and (*d*) NL_LRN.

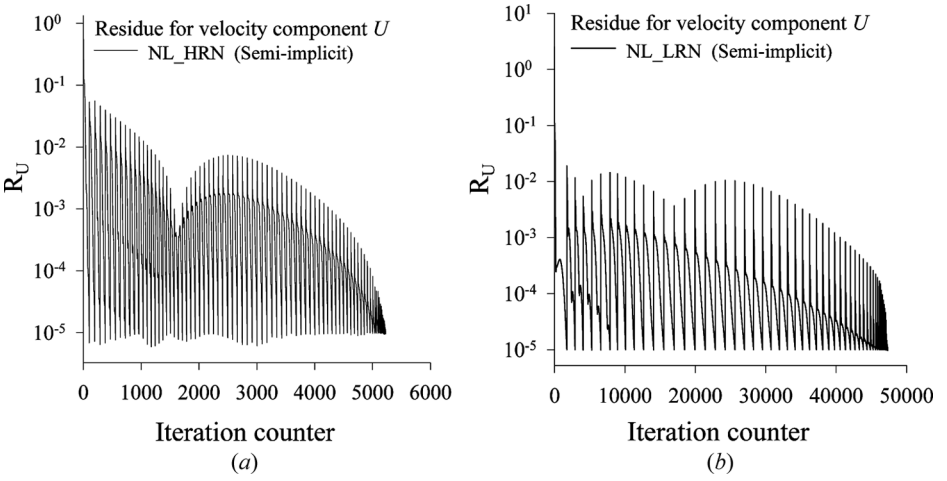

Figure 10. Residue for velocity U. Case symmetric converging-diverging channel. Semi-implicit treatment. (*a*) NL_HRN and (*b*) NL_LRN.

developed condition. As can be seem in Figure 11*a*, the use of the high Reynolds model along with the semi-implicit treatment caused the solution to converge, whereas employment of the explicit approach yielded unstable and diverging solutions (note line with open circles for R_U after only a few iterations). Applying further the low Reynolds model to the same geometry, both the explicit method (not shown in Figure 11*b*) and the implicit treatment converged at a same rate. When looking at all results so far, one can speculate about an intricate interplay of the distinct solution characteristics, such as the sophistication of the turbulence model, and

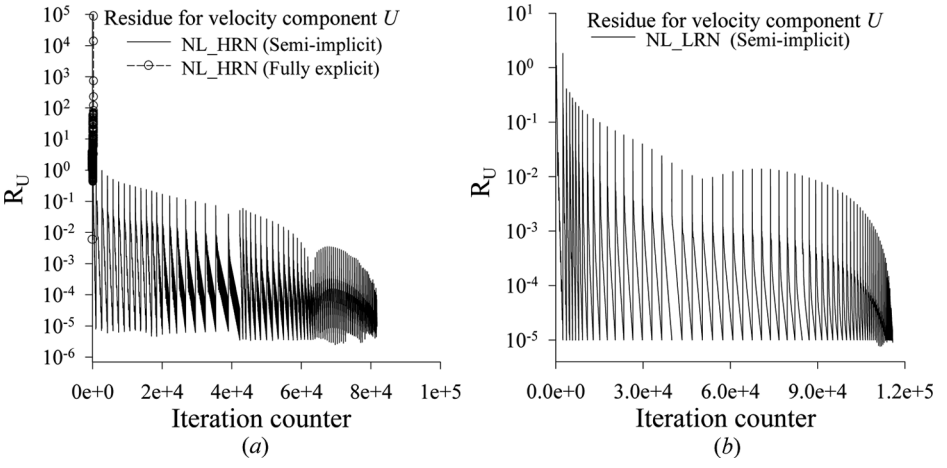

Figure 11. Residue for velocity U for the channel with concave-convex walls. (*a*) NL_HRN – Fully explicit versus semi-implicit treatment and (*b*) NL_LRN – semi-implicit treatment.

the degree of implicitness of the discretization equation and the geometry of the flow. One can say that, when using cheaper and less involving HRNs, a higher degree of implicitness might be necessary in order to obtain stable solutions. Figure 11, in the end, shows that a higher degree of implicitness might be mandatory to achieve convergence in certain situations, as in the cases of concave-convex channels computed with HRN closures.

CONCLUSION

In this work, the performance of four turbulence models was investigated. The analysis was conducted to predict the turbulent flow field at Reynolds number of 40,000 in two periodically sinusoidal-wave channels. The low Reynolds number formulation utilized in the linear and nonlinear k-ε models presented better agreement (for pressure drop) with the experimental data by Saniei and Dini [18], as shown in Table 2. The smallest deviations were obtained with NL_LRN model.

An analysis of residue for the velocity component U along the solution relaxation process was done. It has been observed that for the symmetric converging-diverging channel, the semi-implicit treatment of nonlinear diffusive terms did not benefit the stability characteristics of the solution in relation to the fully explicit treatment when using either the high or the low Reynolds formulation. Both treatments converged at the same rate. For the second geometry investigated, namely the concave-convex wall channel of Figure 2*b*, great difficulty was experimented when pursuing the numerical solutions by means of the nonlinear model. Results indicate that when the high Reynolds wall-treatment is employed, the only way to get a converged solution is to apply the implicit technique here described, which constitutes an advantage of the method herein proposed. For the low Re model, either the explicit or the semi-implicit discretization techniques provided converged solutions with similar rates of convergence.

Ultimately, this work has shown that many factors affect the accuracy and stability of the solution, namely the sophistication of the turbulence model, the degree of implicitness of the solution procedure and the domain geometry, among possible other factors. Further, the semi-implicit approach here proposed has shown to be advantageous in situations were a fully explicit treatment of the diffusive term was inadequate for solution stability. Finally, results herein indicate that for certain classes of flows, appropriate models and discretization techniques may suffice, whereas for flows with strong pressure variation along the flow, such as the one in Figure 2*b*, strong flow deceleration and posterior acceleration may require care when selecting a proper discretization technique for solutions stability and convergence. Therefore, the semi-implicit method here proposed represents an alternative path to numerical analysts when engaged in solving turbulent flows of hard convergence characteristics.

In essence, the main contribution of this work was to show that by implicitly treating sources and diffusion fluxes, solutions using nonlinear models and high Reynolds wall treatment are more stable and easier to be obtained, even with coarser grids and greater relaxation parameters. Ultimately, the technique described here contributes to the always desirable combination of accuracy and economy of numerical solutions of turbulent flows.

REFERENCES

1. S. Ergin, M. Ota, and H. Yamaguchi, Numerical Study of Periodic Turbulent Flow through a Corrugated Duct, *Numer. Heat Transfer A*, vol. 40, no. 2, pp. 139–156, 2001.
2. A. Hadjadj and M. El Kyal, Effect of Two Sinusoidal Protuberances on Natural Convection in a Vertical Concentric Annulus, *Numer. Heat Transfer A*, vol. 36, no. 3, pp. 273–289, 1999.
3. N. Mohamed, B. Khedidja, Z. Belkacem, and D. Michel, Numerical Study of Laminar Forced Convection in Entrance Region of a Wavy Wall Channel, *Numer. Heat Transfer A*, vol. 53, no. 1, pp. 35–52, 2008.
4. S. Prétot, J. Miriel, Y. Bailly, and B. Zeghmati, Visualization and Simulation of the Natural-Convection Flow above Horizontal Wavy Plates, *Numer. Heat Transfer A*, vol. 43, no. 3, pp. 307–325, 2003.
5. L. Z. Zhang and J. L. Niu, A Numerical Study of Laminar Forced Convection in Sinusoidal Ducts with Arc Lower Boundaries under Uniform Wall Temperature, *Numer. Heat Transfer A*, vol. 40, no. 1, pp. 55–72, 2001.
6. E. Nobile, F. Pinto, and G. Rizzetto, Geometric Parameterization and Multiobjective Shape Optimization of Convective Periodic Channels, *Numer. Heat Transfer B*, vol. 50, no. 5, pp. 425–453, 2006.
7. C. Nonino and G. Comini, Finite-Element Analysis of Convection Problems in Spatially Periodic Domains, *Numer. Heat Transfer B*, vol. 34, no. 4, pp. 361–378, 1998.
8. S. H.-K. Lee and Y. Jaluria, Effects of Streamwise Convergence in Radius on the Laminar Forced Convection in Axisymmetric Ducts, *Numer. Heat Transfer A*, vol. 28, no. 1, pp. 19–38, 1995.
9. K. Noto, T. Miyake, and T. Nakajima, Generation of the Karman Vortex Street at Low Reynolds Number due to Cooling a Cylinder: Cause and Fluid Type Effect by Numerical Computation, *Numer. Heat Transfer A*, vol. 40, no. 6, pp. 659–688, 2001.
10. N. H. Saeid and Y. Yaacob, Natural Convection in a Square Cavity with Spatial Side-Wall Temperature Variation, *Numer. Heat Transfer A*, vol. 49, no. 7, pp. 683–697, 2006.
11. S. M. Aminossadati and B. Ghasemi, Comparison of Mixed Convection in a Square Cavity with an Oscillating Versus a Constant Velocity Wall, *Numer. Heat Transfer A*, vol. 54, no. 7, pp. 726–743, 2008.
12. Q.-H. Deng and J.-J. Chang, Natural Convection in a Rectangular Enclosure with Sinusoidal Temperature Distributions on Both Side Walls, *Numer. Heat Transfer A*, vol. 54, no. 5, pp. 507–524, 2008.
13. V. C. Patel, J. T. Chon, and J. Y. Yoon, Turbulent Flow in a Channel with a Wavy Wall, *J. Fluids Eng.*, vol. 113, pp. 579–586, 1991.
14. M. A. Habib, I. Ul-Haq, H. M. Badr, and S. A. M. Said, Calculation of Turbulent Flow and Heat Transfer in Periodically Converging-Diverging Channels, *Computers & Fluids*, vol. 27, no. 1, pp. 95–120, 1998.
15. S. T. Hsu and J. F. Kennedy, Turbulent Flow in Wavy Pipes, *J. Fluid Mech.*, vol. 47, no. 3, pp. 481–502, 1971.
16. D. P. Zilker, G. W. Cook, and T. J. Hanratty, Influence of the Amplitude of a Solid Wavy Wall on a Turbulent Flow, Non-Separated Flows, Part 1, *J. Fluids Mech.*, vol. 82, pp. 29–51, 1977.
17. J. Buckels, T. J. Hanratty, and R. J. Adrian, Turbulent Flow over Large Amplitude Wavy Surfaces, *J. Fluid Mech.*, vol. 140, pp. 27–44, 1984.
18. N. Saniei and S. Dini, Effects of Height and Geometry on Local Heat Transfer and Pressure Drop in Channel with Corrugated Walls, *Heat Transfer Eng.*, vol. 14, no. 4, pp. 19–31, 1993.

19. T. J. Hanratty, J. Abrams, and K. A. Frederic, Flow over Solid Wavy Surfaces, in R. Dumas and L. Fulachier (eds.), *Structure of Complex Turbulent Shear Flow, IUTAM Symposium Marseille 1982*, pp. 79–88, Springer, Berlin, 1983.
20. W. P. Jones and B. E. Launder, The Prediction of Laminarization with Two-Equation Model of Turbulence, *Int. J. Heat & Mass Transfer*, vol. 15, pp. 301–314, 1972.
21. B. E. Launder, G. J. Reece, and W. Rodi, Progress in the Development of a Reynolds Stress Turbulence Closure, *J. Fluid Mech.*, vol. 68, pp. 537, 1975.
22. C. G. Speziale, On Nonlinear k-l and k-ε Models of Turbulence, *J. Fluid Mech.*, vol. 176, pp. 459–475, 1987.
23. S. Nisizima and A. Yoshizawa, Turbulent Channel and Couette Flows Using an Anisotropic k-ε Model, *AIAA J.*, vol. 25, no. 3, pp. 414, 1987.
24. R. Rubinstein and J. M. Barton, Renormalization Group Analysis of the Stress Transport Equation, *Phys. Fluids*, vol. A2, no. 8, pp. 1472–1476, 1990.
25. T. H. Shih, J. Zhu, and J. L. Lumley, A Realizable Reynolds Stress Algebraic Equation Model, NASA TM-105993, 1993.
26. T. B. Gatski and C. G. Speziale, On Explicit Algebraic Stress Models for Complex Turbulent Flows, *J. Fluid Mech.*, vol. 254, pp. 59–78, 1993.
27. R. Abid, C. Rumsey, and T. B. Gatski, Prediction of Nonequilibrium Turbulent Flows with Explicit Algebraic Stress Models, *AIAA J.*, vol. 33, no. 11, pp. 2026–2031, 1995.
28. M. Rahman, P. Rautaheimo, and T. Siikonen, Numerical Study of Turbulent Heat Transfer from a Confined Impinging Jet using a Pseudo-Compressibility Method, in K. Hanjalic and T. Peeters, (eds.), *Turbulence, Heat and Mass Transfer 2*, pp. 511–520, Delf University Press, Delft, 1997.
29. W. Bauer, O. Haag, and D. K. Hennecke, Accuracy and Robustness of Nonlinear Eddy Viscosity Models, *Int. J. Heat and Fluid Flow*, vol. 21, pp. 312–319, 2000.
30. K. Abe, Y. Nagano, and T. Kondoh, An Improved k-ε Model for Prediction of Turbulent Flows with Separation and Reattachment, *Trans. JSME Ser. B*, vol. 58, pp. 3003–3010, 1992.
31. B. E. Launder and D. B. Spalding, The Numerical Computation of Turbulent Flows, *Comp. Meth. Appl. Mech. Eng.*, vol. 3, pp. 269–289, 1974.
32. S. B. Pope, A More General Effective-Viscosity Hypothesis, *J. Fluid Mech.*, vol. 72, pp. 331, 1975.
33. S. V. Patankar, *Numer. Heat Transfer and Fluid Flow*, Hemisphere, New York, 1980.
34. M. J. S. de Lemos, Flow and Heat Transfer in Rectangular Enclosures Using A New Block-Implicit Numerical Method, *Numer. Heat Transfer B*, vol. 37, no. 4, pp. 489–508, 2000.
35. M. J. S. de Lemos, A Block-Implicit Method for Numerical Simulation of Swirling Flows in a Model Combustor, *Int. Comm. Heat And Mass Transfer*, vol. 30, no. 3, pp. 369–378, 2003.
36. M. J. S. de Lemos, A Block-Implicit Numerical Procedure for Simulation of Buoyant Swirling Flows in a Model Furnace, *Int. J. Num. Methods in Fluids*, vol. 43, no. 3, pp. 281–299, 2003.
37. P. K. Khosla and S. G. Rubin, A Diagonally Dominant Second-Order Accurate Implicit Scheme, *Comp. Fluids*, vol. 2, no. 12, pp. 207, 1974.
38. M. Assato and M. J. S. de Lemos, Development of a Non-Linear Turbulence Model for Recirculating Flows Using Generalized Coordinates, ENCIT98, *Proc. 7th Braz. Cong. Eng. Th. Sci.*, vol. 2, pp. 1386–1391, Rio de Janeiro, RJ, Nov. 3–6, 1998.
39. M. Assato and M. J. S. de Lemos, Numerical Simulation of Turbulent Flow Through Axisymmetric Stenosis Using Linear and Non-Linear Eddy-Viscosity Models, *Proc. 16th Brazilian Congress of Mechanical Engineering*, Uberlândia/MG, Brazil, 2001.

40. M. Assato, M. H. J. Pedras, and M. J. S. de Lemos, Numerical Solution of Turbulent Channel Flow Past a Backward-Facing-Step with a Porous Insert Using Linear and Non-Linear k-ε Models, *J. Porous Media*, vol. 8, no. 1, pp. 13–29, 2005.
41. H. L. Stone, Iterative Solution of Implicit Approximations of Multi-Dimensional Partial Differential Equations, *SIAM J. Num. Anal.*, vol. 5, pp. 530–558, 1968.
42. E. J. Braga and M. J. S. de Lemos, Numerical Simulation of Turbulent Flow in Small-Angle Diffusers and Contractions Using a New Wall Treatment and a Linear High Reynolds k-ε Model, *Numer. Heat Transfer A*, vol. 45, no. 9, pp. 911–933, 2004.